


# Infinite-stage Nernst-Ettingshausen Cryocooler for Practical Applications

M. Mobarak Hossain Polash<sup>1,2</sup> and Daryoosh Vashaee<sup>1,2,\*</sup>

<sup>1</sup>*Department of Materials Science and Engineering, North Carolina State University, Raleigh, North Carolina 27606, USA*

<sup>2</sup>*Department of Electrical and Computer Engineering, North Carolina State University, Raleigh, North Carolina 27606, USA*

 (Received 27 June 2020; revised 23 August 2020; accepted 30 November 2020; published 8 January 2021)

Recent developments in Nernst-Ettingshausen (NE) physical phenomena combined with advances in the performance of rare-earth permanent magnets make thermomagnetic (TM) cryocoolers well suited for practical applications. The device performance of a NE cryocooler depends on both the material and the geometric shape of the device. Despite continued progress in TM materials, the optimum shape is still based on a simplified infinite-stage model derived in 1963 by Harman [*Adv. Energy Convers.* 3(4), 667–676 (1963)]. Harman’s model assumes several nonrealistic assumptions, such as temperature-independent material properties and constant current density. We relax such assumptions and derive a fully-temperature-dependent numerical model to accurately solve for the thermomagnetic features of a NE cooler with arbitrary geometry. We correct Harman’s analytical function and compare its performance with the performance of devices of various shapes. The corrected shape has a higher coefficient of performance (COP) at higher temperature differentials, which indicates that when the material resistivity is a strong function of the temperature, the corrected infinite-stage device can provide better performance than Harman’s geometry. Moreover, the corrected infinite-shape device can provide higher heat flow density under a similar optimum-COP condition. A case study based on a state-of-the-art TM material, Bi-Sb alloy, is presented, and the critical parameters for designing an efficient thermomagnetic cooler are discussed in detail.

DOI: [10.1103/PhysRevApplied.15.014011](https://doi.org/10.1103/PhysRevApplied.15.014011)

## I. INTRODUCTION

Solid-state coolers such as thermoelectric (TE) coolers based on the Peltier-Seebeck effect and thermomagnetic (TM) coolers based on the Nernst-Ettingshausen (NE) effect have attracted much attention as competitive green technologies for next-generation cooling applications over the conventional methods owing to their near-zero ozone-depletion potential and global-warming potential [1–4]. Moreover, these devices offer many salient features, such as a long lifetime, high reliability, no moving parts, low maintenance cost, flexible form factor, small size, efficient localized cooling, light weight, fast and dynamic response, good thermal control, noise- and vibration-free application, which helps to increase the resolution of cooled infrared focal-plane arrays (FPAs), no refrigerants, and cost-competitiveness [5,6]. Solid-state coolers are linearly coupled systems governed by Onsager’s theorem, where the entropy is carried by charge, heat, and spin carriers (spin or spin wave) of the system in the presence or absence of a magnetic field via diffusive and advective transport processes [7–10]. Each type of solid-state

cooler has its own efficient operating temperature range [6,11]. Among them, TM devices show better performance in the cryogenic temperature range (below 200 K) [6,11]. Compared with Peltier or TE coolers, TM or NE coolers provide higher temperature differentials in the cryogenic temperature range, which can be further increased by cascading. TE or Peltier coolers can achieve a large temperature differential with multistage cascading, which is practically limited to five or six stages [11]. Moreover, NE coolers have smaller losses due to lower contact resistance compared with TE coolers. The device performance of NE cryocoolers depends on both the shape of the device and the material properties under a transverse magnetic field [6,11]. Recent findings of exotic thermomagnetic effects in different materials [12–15] show huge prospects for improving the thermomagnetic performance from a material perspective, which has revived research on NE cryocoolers. However, fewer studies [6,16–18] have addressed the contribution of the geometric shape of NE devices to enhance their performance. Until now, the infinite-stage shape, derived in 1963 by Harman [19], has been considered the optimum shape for the cascade structure. Harman’s model is based on some idealistic assumptions of temperature-independent material properties and,

\*dvashae@ncsu.edu

therefore, temperature-independent current density. This assumption introduced excess Joule heating, and therefore there is a possibility to optimize the infinite-stage shape further by using more-realistic considerations.

Infinite-stage cascading can improve the performance of NE coolers by increasing the cross-section area in the direction of the heat flow, which increases the heat-pumping capacity of the successive stages [20]. Infinite-stage cascading is not possible for TE devices. But an infinite-stage NE cooler can be built from a single block of material, as there is no need for electrical isolation between the stages [20]. The need for permanent magnets may make these devices bulky and costly. However, with the invention of strong rare-earth magnets, magnetic fields as high as 0.6 T are accessible with reasonably sized magnets [21,22]. In general, solid-state coolers suffer from low efficiency due to low the figure of merit ( $zT$ ) resulting from the counter-indicative properties that define  $zT$ , such as electrical conductivity, thermal conductivity, Seebeck coefficient, and Nernst coefficient [6,11,23,24]. In NE devices,  $zT$  has a  $T^{7/2}$  dependence; hence, it drops more quickly with decrease of temperature [25]. Low  $zT$  reduces the efficiency of the solid-state cooler below that of vapor compression-based coolers [5,6]. Several TE and TM devices were found to be promising for cryogenic applications [26–29], but more research is needed to improve the performance of these devices further to meet application needs.

Recent research on solid-state coolers is mostly focused on discovering TE materials with high  $zT$  [30,31]. Compared with TE materials and devices, less research has been conducted on TM materials and devices [32–35]. But the recent resurgence of the need for solid-state cryocoolers has triggered the need to improve the material properties as well as optimize the device structure. Until now, most studies [36–38] on NE device shape were based on Harman’s exponential shape, ignoring the conceptual approximations in deriving the exponential infinite-stage shape [6,37]. This work addresses some limitations of prior studies, such as constant current density and resistivity approximations [19,37]. We develop a corrected version of Harman’s shaping function, considering a variable current density for a constant electric field and temperature-dependent electrical resistivity. A comprehensive comparison of the device parameters is derived in terms of the maximum heat-pump density, coefficient of performance (COP), and transverse temperature gradient among differently shaped devices, including rectangular, trapezoidal, Harman’s infinite-stage geometry, and the corrected infinite-stage geometry. The degree of enhancement among different geometries determines the right shape for a target application as the construction of the infinite-stage device can be costly; hence, it is not always the best solution. We further introduce a numerical engine that can calculate the different device properties considering the

realistic temperature dependence of the material properties for a cooler with an arbitrary shape. The numerical model is applied to calculate the properties of several coolers with different shapes based on the well-known Bi-Sb alloy for TM applications [38,39]. According to the numerical analysis, the corrected geometry has the highest COP when the current density and heat flow have their optimum values. However, in practice, one may desire to increase the cooling power or the heat flow at the cost of lower COP. Under such conditions, the trapezoidal geometry can deliver higher heat flow for a reasonable COP, which is also a more-accessible geometry for fabrication.

## II. DERIVATION OF THE CORRECTED INFINITE-STAGING FUNCTION

The formalism of the corrected infinite-staging function is obtained by following similar steps as in Harman’s method, but with no limiting assumption on the current density. It is convenient to consider infinite-stage device as a combination of many single stages with a parallelepiped geometry, as shown in Fig. 1. In a multistage device, each stage pumps the combination of heat from the previous stage and the Joule heating from the present stage to the next stage [6,20]. Therefore, the following stages must be able to pump more heat, which requires the size of the single-stage element to increase in the heat-flow direction. The general assumptions to derive the size and shape of the successive stages are the energy-conservation principle and the optimum coefficient of performance among the stages [19]. The maximum COP ( $\text{COP}_{Q_{\max}}$ ) and the optimum COP ( $\text{COP}_{\text{opt}}$ ) in NE devices have different definitions.  $\text{COP}_{Q_{\max}}$  is associated with the maximum cooling power,  $Q_{\max}$ ; therefore,  $\text{COP}_{Q_{\max}}$  is not necessarily the highest COP of a NE device.  $\text{COP}_{\text{opt}}$  is associated with the highest COP of the device. At the optimum COP, the device operates at an economical current but with a lower heat flow rate. Therefore, the cooling power may be too small to provide any useful cooling, which may not be desired for many applications.

Following Harman’s derivation technique (see the Appendix for more details), the primary differential relation among power ( $P$ ), rate of heat flow ( $\dot{\epsilon}$ ), and temperature ( $T$ ) can be expressed as [19]

$$\frac{dP}{P} = \frac{d\dot{\epsilon}}{\dot{\epsilon}} = \frac{dT}{TF^i(\delta)}. \quad (1)$$

Here,  $F(\delta)$  is derived from the COP of a single-stage rectangular device as [19,40]

$$C = \frac{T_0}{\Delta_x T} \frac{[1 - \delta(T_L/T_0)]}{(1 + \delta)} = \eta_c F(\delta), \quad (2)$$

where  $C$  is the COP,  $\eta_c$  denotes the Carnot efficiency of the device and  $F(\delta)$  is a function of  $\delta$ , where  $\delta =$

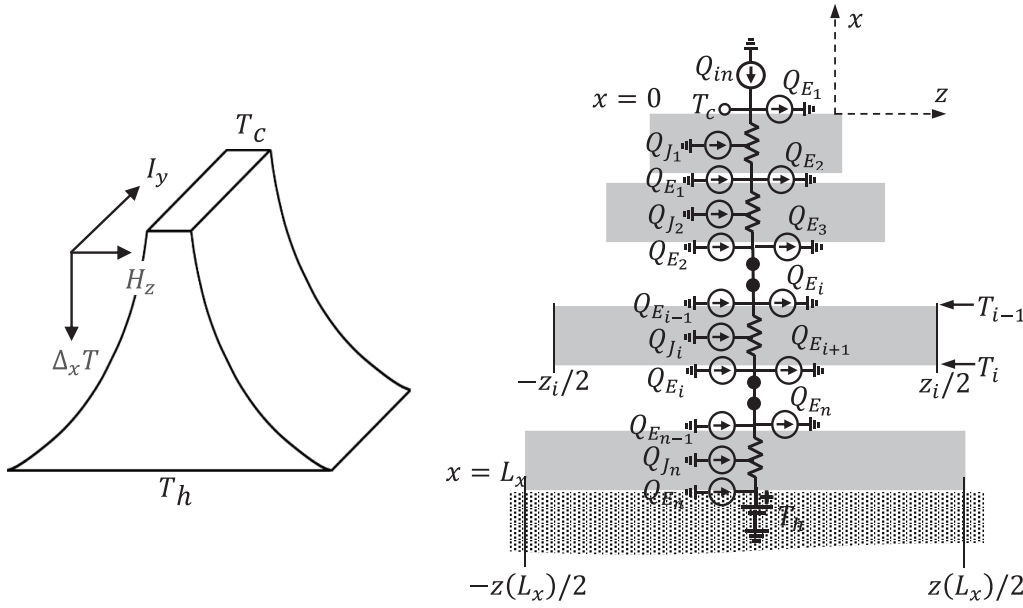


FIG. 1. Infinite-stage NE device along with the direction of the magnetic field, current flow, and temperature gradient (left), and representation of an infinite-stage device with single-staged parallelepiped NE elements along with corresponding equivalent-circuit model (right).

$(1 - z_{NE} \bar{T})^{1/2}$ .  $z_{NE}$  is the thermomagnetic figure of merit expressed as [20]

$$z_{NE} = \frac{(\alpha_{yx} + H_z N_{yx})^2}{\kappa_{xx} \rho_{yy}}, \quad (3)$$

where  $\alpha_{yx}$  is the magneto-Seebeck coefficient along the  $y$ - $x$  plane (a negligible term that is often ignored in the literature),  $H_z$  is the magnetic field in the  $z$  direction,  $N_{yx}$  is the Nernst coefficient in the  $y$ - $x$  plane,  $\kappa_{xx}$  is the thermal conductivity in the  $x$  direction, and  $\rho_{yy}$  is the electrical resistivity in the  $y$  direction.

Four different types of figure of merit ( $z_{NE}$ ) are found in the literature [37,41]. The differences are due to the isothermal or adiabatic material properties. The first definition is  $z_{NE} = (H_z N_{yx})^2 / \rho_{yy} \kappa_{xx}$ , where the material properties are isothermal and  $0 \leq z_{NE} \leq 1$ . The second definition is  $z_{NE}^* = (H_z N_{yx})^2 / \rho_{yy} \kappa_{xx}^* = z_{NE} / (1 + z_{NE} T)$ , where  $\kappa_{xx}^* \equiv \kappa_{xx} (1 + z_{NE} T)$ , and always  $z_{NE}^* T < 1$ . In most experiments, one measures  $\kappa_{xx}^*$  because there is usually no load connected to the sample (hence,  $J_{yy} = 0$ ), and  $\kappa_{xx}^*$  includes transverse corrections due to the Nernst effect on electrical conductivity and the Ettingshausen effects [41]. The third definition is the adiabatic Ettingshausen figure of merit, which assumes adiabatic resistivity; that is,  $\rho_{yy}^a = \rho_{yy} / (1 + z_{NE} T)$ , and hence  $z_{NE}^a = (H_z N_{yx})^2 / \rho_{yy}^a \kappa_{xx}^a$ .  $z_{NE}^a$  can take any value from zero to infinity. Finally, another Ettingshausen figure of merit considers  $\rho_{yy}^a$  and  $\kappa_{xx}^*$ ; therefore, the fourth figure of merit is  $z_{NE}^{a*} = (H_z N_{yx})^2 / \rho_{yy}^a \kappa_{xx}^*$ . Since  $\rho_{yy}^a \kappa_{xx}^* = \rho_{yy} \kappa_{xx}$ , we have  $z_{NE}^{a*} = z_{NE}$ . Because of the existence of different definitions of  $z_{NE}$ , it is vital to understand which  $z_{NE}$  is used in formulating the device operation and performance. Experimentally, one usually measures  $\rho_{yy}^a$  and  $\kappa_{xx}^*$ . Therefore, the experimental figure of merit is  $z_{NE}^{a*}$ ;

that is,  $z_{NE} \leq 1$ . Theoretically, one usually calculates the thermal conductivity  $\kappa_{xx}$  and  $\rho_{yy}$ ; therefore, the theoretical figure of merit is  $z_{NE} \leq 1$ .

In the following, we assume isothermal quantities for all material properties  $\kappa_{xx}^*$ ,  $\rho_{yy}$ , and  $N_{yx}$ ; that is, they are the values measured for zero temperature gradient unless a temperature gradient in a direction is needed for the measurement. Furthermore, we use  $\kappa_{xx}^*$  and  $z_{NE}^*$  in the equations. However, for convenience, we drop the asterisk superscript from this point. As NE devices are usually assumed to be a transverse isothermal cooler, there is no heat flow in the  $y$  and  $z$  directions; therefore, the device is generally made long in the  $y$  direction with respect to the  $x$  direction [20]. The net input power in the  $i$ th stage, which is the difference between the input and output energy flow rates, can be expressed as [19]

$$P^i = 2z \Delta x^i L_y E_y^i J_y^i. \quad (4)$$

Similarly, for the next stage,  $(i+1)$ th, the input power is [19]

$$P^{i+1} = 2(z + \Delta z) \Delta x^{i+1} L_y E_y^{i+1} J_y^{i+1}, \quad (5)$$

where  $\Delta x$  is the height,  $L_y$  is the length,  $z$  is the width of the corresponding stage, and  $\Delta z$  is the increase of the size in the  $z$  direction with respect to the previous stage. For multistage devices, where all stages are physically connected, it is reasonable to consider that the electric field across all stages must be the same. However, the current through each stage can be different because the stages are at different temperatures, and the electrical conductivity is a function of the temperature. To obtain the optimum geometry, it is also essential to optimize the individual stages for the corresponding current density and voltage gradient

[19]. The expressions for the current density and the voltage gradient for the optimized shaped device are given by [19]

$$J_y = -\frac{\kappa_{xx}}{H_z N_{yx}} \frac{\Delta_x T (1 + \delta)}{T \Delta x}, \quad (6)$$

$$E_y = -H_z N_{yx} \frac{\Delta_x T}{\Delta x} \frac{\delta}{(1 - \delta)}. \quad (7)$$

Here it is imperative to mention that different expressions for optimum current densities were reported by Harman [19] and Hawkins et al. [20], but are essentially the same as each other. From the expressions for the electric field and the current density for the optimized shaped device, the temperature-dependent Ohm's law for the NE device can be expressed as

$$J_y = \frac{1}{\rho_{yy} \sqrt{1 - z_{NE} T}} E_y. \quad (8)$$

Resistivity usually has a reciprocal relation with temperature [37]; however, an exponential relationship is more suitable for  $\text{Bi}_x\text{Sb}_{1-x}$  semimetals in the cryogenic temperature range because the resistivity is mainly a function of the carrier concentration, and the carrier excitation follows an exponential function versus temperature. A good exponential fit to the experimental data is shown in Fig. 2. Since a good thermomagnetic material must have a low extrinsic carrier concentration, the exponential-relationship assumption is expected to be generally valid for other thermomagnetic coolers too. Therefore, the exponential function is used in the subsequent model calculations. According

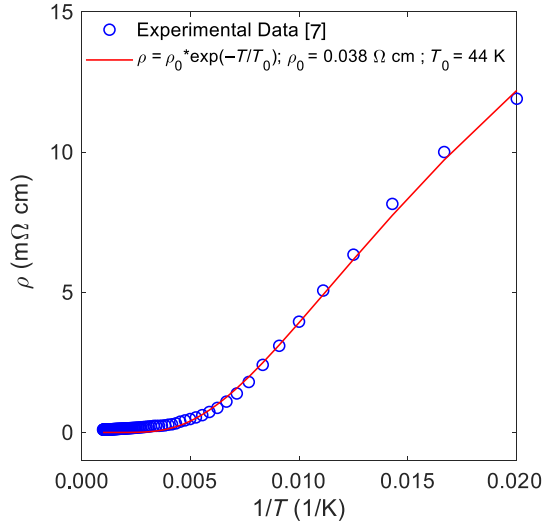


FIG. 2. Resistivity (blue circles) of  $\text{Bi}_{97}\text{Sb}_3$  as a function of reciprocal temperature and the corresponding exponential fit (red line).

to this consideration, the resistivity in the temperature range of interest (Fig. 2) may be written as  $\rho = \rho_0 e^{-T/T_0}$ , where  $\rho_0$  and  $T_0$  are material-dependent constants. Replacing  $\rho$  in Eq. (8), we can write the expression for the temperature-dependent Ohm's law for the  $i$ th stage as

$$J_y = \frac{e^{T_i/T_0}}{\rho_0 \sqrt{1 - zT}} E_y^i. \quad (9)$$

Assuming  $zT$  is a temperature-independent parameter and  $E_y$  is constant for each stage, we can write the current density for the  $(i+1)$ th stage with respect to the  $i$ th stage as

$$J_y^{i+1} = \frac{e^{T_{i+1}/T_0}}{\rho_0 \sqrt{1 - zT}} E_y^{i+1} = e^{(T_{i+1}-T_i)/T_0} J_y^i. \quad (10)$$

Simplifying Eq. (10), we can express the ratio of the current densities of the  $(i+1)$ th and  $i$ th stages as

$$\frac{J_y^{i+1}}{J_y^i} = e^{(T_{i+1}-T_i)/T_0} = 1 + \frac{\Delta T}{T_0}, \quad (11)$$

where  $\Delta T = T_{i+1} - T_i$ . To obtain the differential relation of Eq. (1), we can use Eqs. (4), (5), and (10):

$$\frac{P^{i+1} - P^i}{P^i} = \frac{2(z + \Delta z) \Delta x^{i+1} L_y E_y^i J_y^{i+1} - 2z \Delta x^i L_y E_y^i J_y^i}{2z \Delta x^i L_y E_y^i J_y^i}. \quad (12)$$

Using Eq. (10), we can simplify the above expression by assuming a similar height ( $\Delta x$ ) for all the stages:

$$\frac{P^{i+1} - P^i}{P^i} = \frac{\Delta P}{P} = \left(1 + \frac{\Delta z}{z}\right) \left(1 + \frac{\Delta T}{T_0}\right) - 1. \quad (13)$$

Ignoring the second-order-derivative terms after factor multiplication, we can derive the following expression from Eq. (13):

$$\frac{\Delta P}{P} = \frac{\Delta z}{z} + \frac{\Delta T}{T_0}. \quad (14)$$

Finally, from Eqs. (1) and (14), we can get the following differential relation:

$$\frac{dP}{P} = \frac{dz}{z} + \frac{dT}{T_0} = \frac{d\epsilon}{\epsilon} = \frac{dT}{TF(\delta)} = b, \quad (15)$$

where  $b$  is an arbitrary constant. To operate a multi-stage device at its optimum COP, one must adjust the intermediate-stage temperatures according to the following

relation [19]:

$$\frac{\Delta T^i}{\Delta x^i T^{i-1}} = \frac{\Delta T^{i+1}}{\Delta x^{i+1} T^i} = b', \quad (16)$$

where  $b'$  is another constant. Taking  $b'$  equal to  $bF(\delta)$ , we can write a generalized expression for Eq. (16) as [19]

$$\frac{dT}{TF(\delta)} = bdx. \quad (17)$$

From Eqs. (15) and (17), the following expression can be derived:

$$\frac{dz}{z} = bdx - \frac{dT}{T_0}. \quad (18)$$

By integration of both sides of Eq. (18), we get

$$\ln z = bx - \frac{T}{T_0} + c, \quad (19)$$

where  $c$  is a constant. Applying the boundary conditions (i.e.,  $T = T_c$  at  $x = 0$  and  $T = T_h$  at  $x = L_x$ ), we can find  $b$  and  $c$ . By inserting them in Eq. (19), we can write

$$\ln \frac{z(x)}{z(0)} = \frac{x}{L_x} \ln \frac{z(L_x)}{z(0)} + \frac{x}{L_x} \frac{T_h - T_c}{T_0} - \frac{T - T_c}{T_0}. \quad (20)$$

Equation (20) is the corrected function for the infinite-stage geometry, whereas Harman's shaping function [19] is

$$\ln \frac{z(x)}{z(0)} = \frac{x}{L_x} \ln \frac{z(L_x)}{z(0)}. \quad (21)$$

We can introduce the corrected shaping function as

$$\ln \frac{z(x)}{z(0)} = \frac{x}{L_x} \ln \frac{z(L_x)}{z(0)} + \theta, \quad (22)$$

in which the correction term,  $C$ , is

$$\theta = \frac{x}{L_x} \frac{T_h - T_c}{T_0} - \frac{T - T_c}{T_0}. \quad (23)$$

According to the above expression,  $\theta$  has a contribution from temperature-dependent and material property-dependent corrections. From Eq. (23), it can be seen that the hot-side temperature, the cold-side temperature, the device length, the spatial temperature profile of the device, and the parameter  $T_0$  can cause the optimum shape of the multistage device to deviate from that obtained with Harman's shaping function. The corrected infinite-stage function can be reduced to Harman's infinite-stage function with  $dT = 0$ .

### III. NUMERICAL FRAMEWORK

In this section, we develop a generalized numerical model based on the device fundamental equations [40]. All material properties are assumed to be temperature dependent. The model is solved to analyze and compare the different geometries of the NE coolers. The numerical framework is based on the thermodynamic relations of a single-stage parallelepiped NE device [40], which is then extended to include the current density and spatial temperature distribution along the  $x$  direction of a cooler in a self-consistent manner. In transverse isothermal thermomagnetic coolers, the conditions  $\nabla_y T = 0$  and  $J_x = 0$  are usually applied to the thermodynamic relations [40]. The interdependent temperature gradient and the heat flow density of individual stages are self-consistently solved across the target geometry. An equivalent-electrical-circuit model (shown in Fig. 1) is used to simplify the calculations. In this model, heat flow and temperature are represented by electrical current and voltage sources, respectively. The thermal resistance of each stage is modeled by electrical resistance. The temperature profile across the cooler is calculated iteratively, considering the interdependent heat current density and temperature.

The temperature at the  $j$ th stage can be expressed as

$$T_j = T_{j+1} - R_{\text{th}}^j \times \left( \sum_{i=1}^j Q_{Ec}^i - \sum_{i=1}^{j-1} Q_{Eh}^i - Q_{\text{in}} - \sum_{i=1}^j Q_J^i + \frac{Q_J^j}{2} \right), \quad (24)$$

where  $R_{\text{th}}$  is the thermal resistance of a single stage under the isothermal condition,  $Q_{Ec}$  and  $Q_{Eh}$  are the Ettingshausen heat-flow density at the cold side and at the hot side of a single stage, respectively,  $Q_{\text{in}}$  is the input heat flow density, and  $Q_J$  is the Joule heat flow density.  $R_{\text{th}}$  is calculated from  $R_{\text{th}} = 1/[\kappa_{xx}(1 - z_{\text{NE}}^* T)] \times \Delta x_i / (L_y L_z)$  [20], in which  $T$  is the average temperature of the stage. We consider the second definition of the figure of merit,  $z_{\text{NE}}^*$ , as described earlier, in the calculation of the thermal resistance  $R_{\text{th}}$  and any other device properties. From Eq. (24), the expression for the cold-side temperature can be written as

$$T_c = T_h - \sum_{j=1}^N R_{\text{th}}^j \left( \sum_{i=1}^j Q_{Ec}^i - \sum_{i=1}^{j-1} Q_{Eh}^i \right) + \sum_{j=1}^N R_{\text{th}}^j Q_{\text{in}} + \sum_{j=1}^N R_{\text{th}}^j \sum_{i=1}^j Q_J^i - \frac{1}{2} \sum_{j=1}^N R_{\text{th}}^j Q_J^j. \quad (25)$$

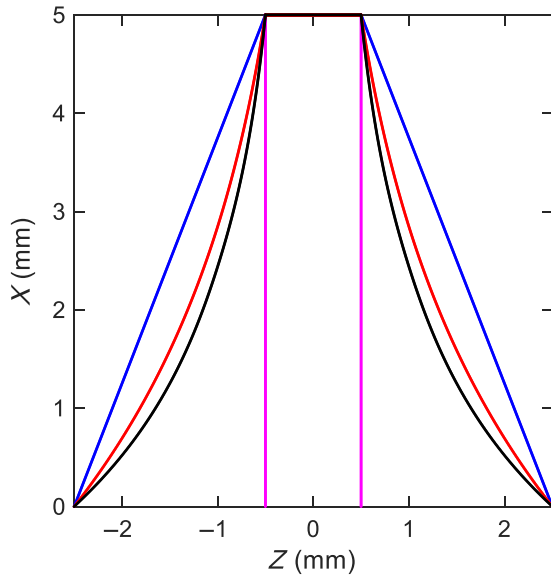


FIG. 3. Different geometries used to compare the performance of NE devices: rectangular (pink), trapezoidal (blue), Harman's infinite stage (red), and temperature-dependent corrected infinite stage (black). The corrected infinite-stage device aligns with Harman's infinite-stage device at  $dT=0$ . With the increase of  $dT$ , the corrected infinite-stage device becomes thinner in the middle. According to Eq. (25), the device length can also affect the deviation of the optimum shape.

Finally, the input heat current density can be expressed as

$$Q_{in} = \frac{1}{\sum_{j=1}^N R_{th}^j} \left[ T_c - T_h + \sum_{j=1}^N R_{th}^j \left( \sum_{i=1}^j Q_{Ec}^i - \sum_{i=1}^{j-1} Q_{Eh}^i \right) - \sum_{j=1}^N R_{th}^j \sum_{i=1}^j Q_J^i + \frac{1}{2} \sum_{j=1}^N R_{th}^j Q_J^j \right]. \quad (26)$$

In the following, we study and compare the performance of differently shaped devices. Figure 3 illustrates the geometries of the devices studied. To compare the different device geometries, we chose the device parameter values as follows:  $L_x = 0.5$  cm,  $L_y = 1$  cm,  $L_z$  at cold side of 0.1 cm,  $T_h = 150$  K, and  $z_{ratio} = 5$ . All devices are divided into 500 single parallelepiped stages. The physical properties of single-crystal  $Bi_{97}Sb_3$  are assumed in the numerical model [20]. The cooling temperature, the heat flow density, and the COP are compared for the different geometries. Furthermore, the COP and  $dT/T$  across the device (versus  $x$ ) are calculated to validate the assumptions made in our deriving the optimum geometry. A detailed discussion is presented in the following section.

#### IV. RESULTS AND DISCUSSION

The device characteristics are calculated numerically by our using temperature-dependent material properties of

single-crystal  $Bi_{97}Sb_3$ . Quite often, in the literature, only the temperature difference is reported as a function of current for different hot-side temperatures [20,38], and the COP or heat flow densities are usually ignored due to their complicated calculations [20]. Therefore, we demonstrate the usefulness of the model by calculating all three quantities for different geometries and under different conditions. Four different shapes are modeled; namely, a rectangular cuboid, a trapezoidal prism, Harman's infinite stage, and the corrected temperature-dependent infinite-stage device.

Figure 4 illustrates the temperature map of differently shaped NE devices superimposed on their geometric shapes for the maximum temperature difference ( $\Delta T_{max}$ ). In all devices, the hot side is at the bottom of the device, which is kept fixed at 150 K. Therefore, heat flow occurs in a downward direction from the cold side to the hot side. The temperature profiles for different geometries can be compared in Fig. 4. In the rectangular cuboid, the temperature increases more quickly compared with the other geometries below the top surface. Therefore, the cooling performance of the other devices is better than that of the rectangular device.

A similar kind of comparison is demonstrated in Fig. 5, where the temperature variation along the  $x$  axis for all devices is plotted at two temperature differences of  $\Delta T = 0$  K and  $\Delta T_{max}$ . Temperature variation is shown for both maximum heat flow,  $Q_{max}$ , and optimum COP. It can be seen from Fig. 5 that the temperature at any  $x$  point inside the device is higher in the rectangular device compared with the other devices. Therefore, it is expected that the cooling performance of the other devices should be better than that of the rectangular device. Moreover, the spatial temperature profile becomes linear in the infinite-stage devices at  $\Delta T_{max}$ . Generally,  $\Delta T = 0$  K occurs when the device works at its maximum cooling power,  $Q_{max}$ . All Ettingshausen devices, except the corrected infinite-stage device, show higher temperatures inside the device than at the ends under the  $Q_{max}$  condition at  $\Delta T = 0$  K. For  $COP_{opt}$ , the inner temperature of all staged devices, except the rectangular one, drops compared with the end temperatures at  $\Delta T = 0$  K. The temperature-variation trend along the  $x$  axis under the  $\Delta T_{max}$  condition for all devices is in agreement with the observed trends in Fig. 4.

The typical performance indicator for Ettingshausen devices is the temperature difference as a function of the operating current. To evaluate the performances of the devices with different geometric shapes, we plot the temperature difference,  $\Delta T$ , as a function of current in Fig. 6. As expected, the other NE devices provide larger  $\Delta T$  than the rectangular device, which is also confirmed in previous figures. For rectangular devices,  $\Delta T_{max} \approx 36$  K is obtained at 7 A, while  $\Delta T_{max} \approx 50$  K is obtained for the trapezoidal device at 32 A,  $\Delta T_{max} \approx 52$  K is obtained for Harman's infinite-stage device at 25 A, and  $\Delta T_{max} \approx 52.3$  K is obtained for the corrected infinite-stage NE

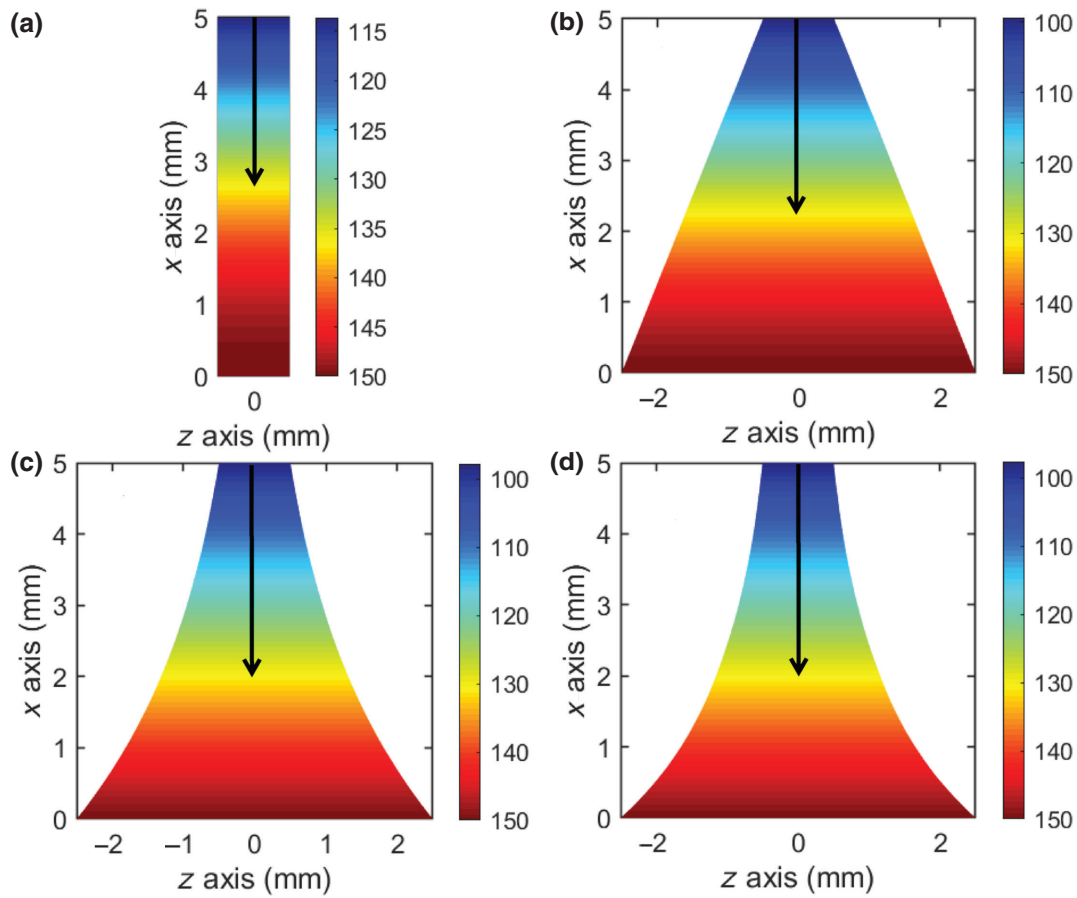


FIG. 4. Spatial temperature map with cooling depth (arrow) at the maximum temperature difference in differently shaped NE devices: (a) thin rectangular cuboid, (b) trapezoidal prism, (c) Harman’s infinite-stage device, and (d) the corrected infinite-stage device. The cold-side and hot-side widths are assumed to be 1 and 5 mm, respectively, and the hot-side temperature is fixed at 150 K.

device at 24 A. The results also show good agreement with previously published data [20,38]. After  $\Delta T_{\max}$ ,  $\Delta T$  decreases with increase of the electrical current due to the

dominancy of Joule heating over Ettingshausen cooling. The corrected infinite-stage device gives a slightly higher  $\Delta T_{\max}$  at a lower current than Harman’s infinite-stage

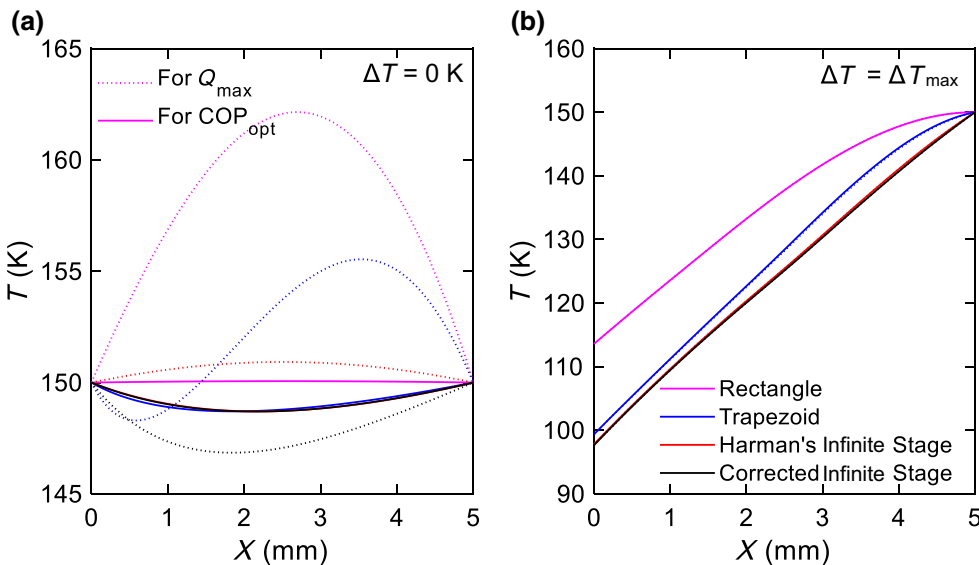


FIG. 5. Temperature variation along the  $x$  axis for different devices at (a)  $\Delta T = 0$  K and (b)  $\Delta T = \Delta T_{\max}$ .

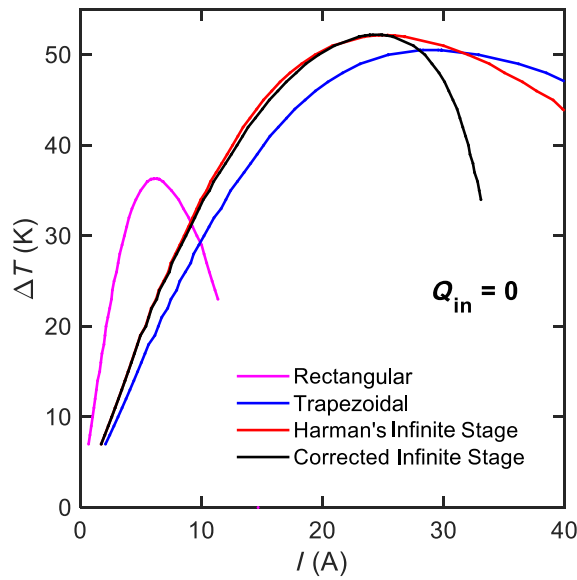


FIG. 6. Temperature difference ( $\Delta T$ ) versus current ( $I$ ) for differently shaped NE devices: rectangular device, trapezoidal device, Harman's infinite-stage device, and the corrected infinite-staged device derived in this work.

device. As discussed later, the corrected infinite-stage device can operate at a simultaneously higher COP and heat flow density compared with the other geometries. Therefore, to evaluate the device performance, the COP and heat flow density are also important parameters along with the highest achievable  $\Delta T$ . Moreover, at maximum  $\Delta T$ , the heat flow density, and hence the COP, is zero. As mentioned earlier, we found no prior reports for the heat flow and the COP of different geometries, so this study can provide a benchmark for future work. Such calculations are comparatively more extensive than  $\Delta T$  and require detailed analysis. In the following, we demonstrate both the COP and the heat flow density for differently shaped devices and compare their performances. Both heat flow and the COP are shown for two temperature differences lower than  $\Delta T_{\max}$ ; namely,  $\Delta T=10$  K and  $\Delta T=50$  K for a low-temperature-difference condition and a high-temperature-difference condition, respectively.

Heat flow density from the cold side to the hot side as a function of the electrical current is calculated at  $\Delta T=10$  K and  $\Delta T=50$  K for all NE devices. Heat flow inside a NE device consists of both Joule and Ettingshausen components, as shown in Fig. 1. The heat flow density for each NE device is higher for smaller  $\Delta T$  as expected, and is shown in Fig. 7(a). With the increase of  $\Delta T$  to 50 K, the heat flow reduces significantly, as shown in Fig. 7(c). At  $\Delta T=50$  K, the heat flow density becomes negative for rectangular NE devices, as  $\Delta T_{\max} \approx 36$  K for this device. Therefore, the heat flow density for the rectangular NE device is not shown in Figs. 7(c) and 7(d). As mentioned earlier, the heat flow density shows a decrease

after a maximum value with increase of the current density, which is related to the domination of Joule heating over Ettingshausen cooling. While the other NE devices show greater heat flow capacity than the rectangular device, the trapezoidal NE device has a higher heat flow density than the infinite-stage devices at  $\Delta T=10$  K, which corresponds to its larger electrical current (larger input power) as shown in Fig. 6. The Ettingshausen heat flow density is proportional to the current, while the Joule heat flow density is proportional to the current squared. Therefore, the heat flow density trend follows the trend of the Ettingshausen heat flow density in the lower current range, and at higher currents, the total heat flow density follows the pattern of Joule heating. The corrected infinite-stage device has a higher heat flow density at around 50 K than the trapezoidal device and Harman's infinite-stage device, and the peak occurs at a lower electrical current, which can be attributed to the more-accurate consideration of Joule heating in our designing this device. At  $\Delta T=10$  K, the corrected infinite-stage NE device also has higher heat flow density than Harman's infinite-stage device at a lower current. As discussed later, this results in a higher COP for the corrected infinite-stage device. Here, it is essential to mention that the corrected infinite-stage device is thinner than both the trapezoidal device and Harman's infinite-stage device; hence, it pumps more heat with less material. According to Eq. (20), the optimum geometry is a function of both  $T_c$  and  $\Delta T$ . Therefore, the corrected infinite-stage NE device optimized for  $\Delta T=50$  K may not be optimum for a different  $\Delta T$  (or  $T_c$ ).

To evaluate the performance of the shaped devices, a comparison of the COP is also critical, as shown in Figs. 7(b) and 7(d). The COP versus current for each shaped device at a given  $\Delta T$  is calculated. Here, the heat flow with respect to the electrical current is adjusted so that  $\Delta T$  remains fixed. At a lower temperature difference ( $\Delta T=10$  K), the rectangular NE device shows a higher  $\text{COP}_{\text{opt}}$  of around 1.35 at 1.8 A with a significantly lower heat flow density (around  $1 \text{ W/cm}^2$ ), which is not desirable for practical applications. However, rectangular devices can provide a higher heat flow density of around  $3.2 \text{ W/cm}^2$  at around 6.7 A and a COP of 0.35. On the other hand, the corrected infinite-stage NE device has a higher  $\text{COP}_{Q_{\max}}$  (around 0.3) at a lower current (around 20 A) than the other NE devices (around 0.2 for both the trapezoidal device and Harman's infinite-stage device). Compared with the trapezoidal NE device, the corrected infinite-stage device gives an around 30% higher COP with around 18% less heat flow density at  $\Delta T=10$  K. Despite showing a higher COP at the low-temperature difference, the COP of the rectangular device drops sharply with the current. At lower  $\Delta T$  and at the  $\text{COP}_{\text{opt}}$ ,  $Q_{\text{opt}}$  is much lower than  $Q_{\max}$ , and all shaped devices provide similar  $Q_{\text{opt}}$  performance. In general, the other NE devices have a higher COP than the rectangular NE device at a particular current



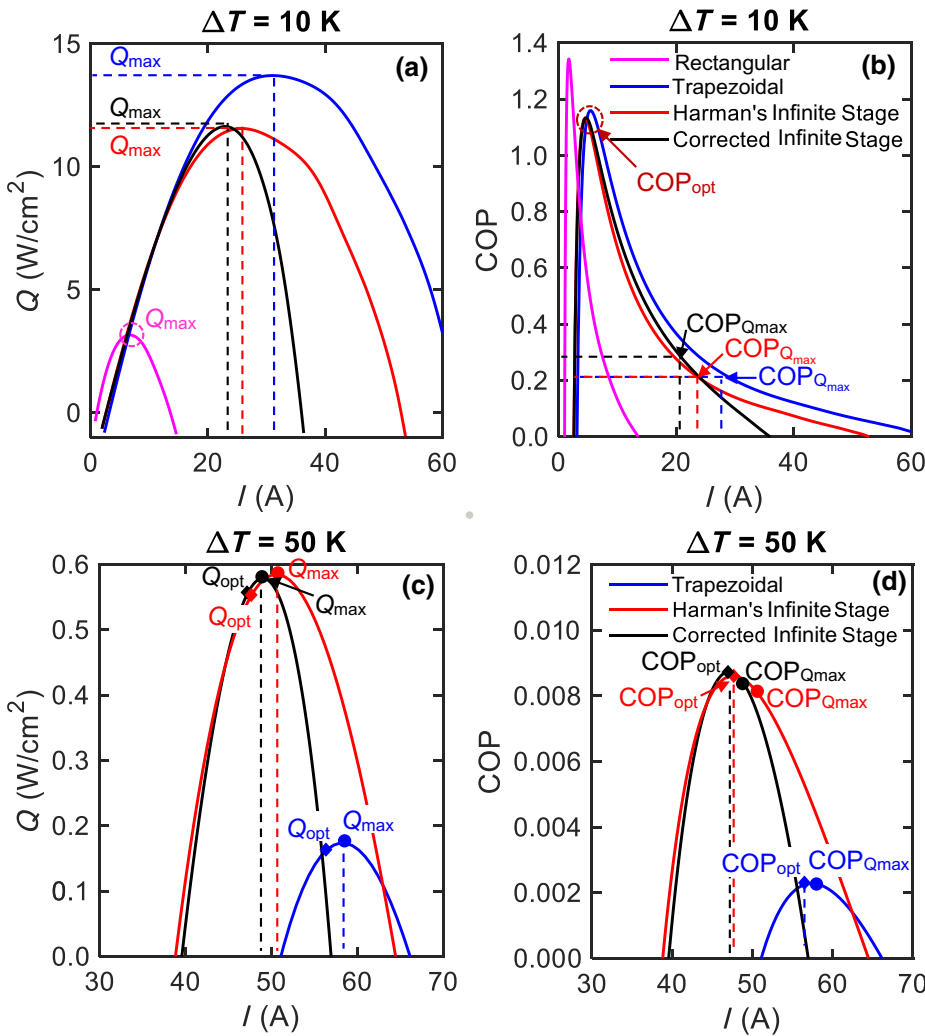


FIG. 7. (a),(c) Heat flow density and (b),(d) COP as a function of driving current for differently shaped NE devices at (a),(b)  $\Delta T = 10$  K and (b),(d)  $\Delta T = 50$  K.

and higher temperature difference, consistent with previous results and theory [20,38]. At 10 K, the trapezoidal device has a slightly higher COP at a slightly higher current with a similar heat flow density, as seen in Figs. 7(a) and 7(b). But, at a larger  $\Delta T$ , the infinite-stage devices show a much larger COP than the trapezoidal device. At 50 K, both infinite-stage devices pump more heat at a lower current than the trapezoidal device (Fig. 7), which results in higher COPs. Moreover, the corrected infinite-stage device can pump slightly more heat at a slightly lower current than Harman's infinite-stage device, which gives it a somewhat higher COP. While the  $\text{COP}_{Q_{\max}}$  for Harman's infinite-stage device is about 0.2 at  $\Delta T = 10$  K, the corresponding value is about 0.28 for the corrected infinite-stage device (i.e., 40% increase). At a temperature difference of 50 K, the corrected infinite-stage device has a  $\text{COP}_{Q_{\max}}$  around 5% higher than Harman's infinite-stage device. Both infinite-stage devices show a similar  $\text{COP}_{\text{opt}}$  with similar  $Q_{\text{opt}}$  performance. As mentioned, the COP can be of two types: namely,  $\text{COP}_{Q_{\max}}$  and  $\text{COP}_{\text{opt}}$ . To determine the optimum operating condition for a NE device, we must consider both the current and the heat flow density.

The heat flow density should be maximized as a function of the current or the desired temperature differential. Then, the corresponding COP is calculated versus the current density and heat flow.

One can see from Fig. 7 that the efficient operation of a NE cooler typically requires a high current at a low voltage. Depending on the cooler's size, the current and voltage scale with the cross section and length of the cooler, respectively. The voltage scales with  $z$ , which does not affect the cross section and hence the optimum current. Indeed, this is one of the advantages of NE coolers compared with TE coolers, as the same current can cool larger areas by one simply scaling the device in the  $z$  direction. The current scales with the cross section in the  $x$ - $y$  plane and can be much smaller for a miniature cooler (e.g., for on-chip cooling of focal plane arrays or electronic devices). The optimum current density is on the order of a few hundred amperes per square centimeter, which is practical for many devices.

Finally, the contact resistance is usually less of an issue for NE coolers compared with TE coolers because (i) NE coolers have only two contacts, while TE coolers have

many, and (ii) NE coolers can be made long (in the  $z$  direction); therefore, their resistance dominates over the contact resistance. For instance, the resistance of the thin rectangular NE cooler ( $5 \times 10 \times 2$  mm<sup>3</sup>) is around  $0.04 \Omega$  at 100 K. The typical metal-semiconductor contact resistance for the given cross section is approximately  $0.00001 \Omega$ , assuming  $\rho = 10^{-6} \Omega \text{cm}^2$ , which is comparatively negligible. According to Fig. 7, rectangular devices can operate at lower current (i.e., 6.7 A for  $Q_{\text{max}}$  or 1.8 A for the  $\text{COP}_{\text{opt}}$  at  $\Delta T = 10$  K). But unlike for the other NE coolers,  $\Delta T$  of the rectangular device is limited by  $(1/2)z_{\text{NE}}T_c^2$  or  $(1/2)z_{\text{NE}}^*T_h^2$  [37,41] independent of the dimensions.

To show the concept of optimum device operating conditions, we illustrate some critical parameters in Fig. 8. Figure 8(a) shows the heat flow density,  $Q$ , which is maximized as a function of the current density for each  $\Delta T$ , Fig. 8(b) provides the COP versus  $\Delta T$  for maximum  $Q$  (i.e.,  $\text{COP}_{Q_{\text{max}}}$ ) and the corresponding current density, and Fig. 8(c) gives the current density that maximizes  $Q$ . On the other hand, Fig. 8(d) shows the heat flow density,  $Q$ , versus  $\Delta T$  that maximizes the COP (i.e.,  $Q_{\text{opt}}$ ) as a function of current density, Fig. 8(e) provides the  $\text{COP}_{\text{opt}}$  versus  $\Delta T$  for optimum  $Q$  and the corresponding current density, and Fig. 8(f) illustrates the current density that optimizes  $Q$ . As expected, the maximum heat flow density and COP both decrease linearly with the increase of  $\Delta T$  and approach

zero at  $\Delta T_{\text{max}}$ . In Fig. 8(b), the rectangular device shows a higher  $\text{COP}_{\text{max}}$  at lower  $\Delta T$ , which is also seen in Fig. 7. Note that the COP is presented as a function of current in Fig. 7, while the  $\text{COP}_{Q_{\text{max}}}$  at  $\Delta T = 10$  K is for the maximum heat flow density at the same temperature difference (shown in Fig. 7). According to Fig. 7, the heat flow density of different NE devices at  $\Delta T = 10$  K is maximized at different currents, which corresponds to different COP values in Fig. 8. In general, a higher  $\text{COP}_{Q_{\text{max}}}$  at a lower temperature difference for the rectangular device is related to its lower current density at the cost of lower heat flow capacity, which is not always desired for practical use. In contrast, the other NE devices can take more heat at the expense of higher current density, which makes them better for higher- $\Delta T$  applications. Importantly, the corrected infinite-stage device always shows a greater COP compared with the other devices, as it carries more heat at less current.

The COP of the trapezoidal device is slightly higher at low  $\Delta T$  values and only marginally lower at high  $\Delta T$  values than that of the infinite-stage devices. Therefore, the trapezoidal device could be a better option for practical applications due to its simpler structure. At high  $\Delta T$  values, the COP of both infinite-stage devices becomes higher due to the higher heat flow at a lower driving current. The performance of the rectangular device shown in Fig. 8

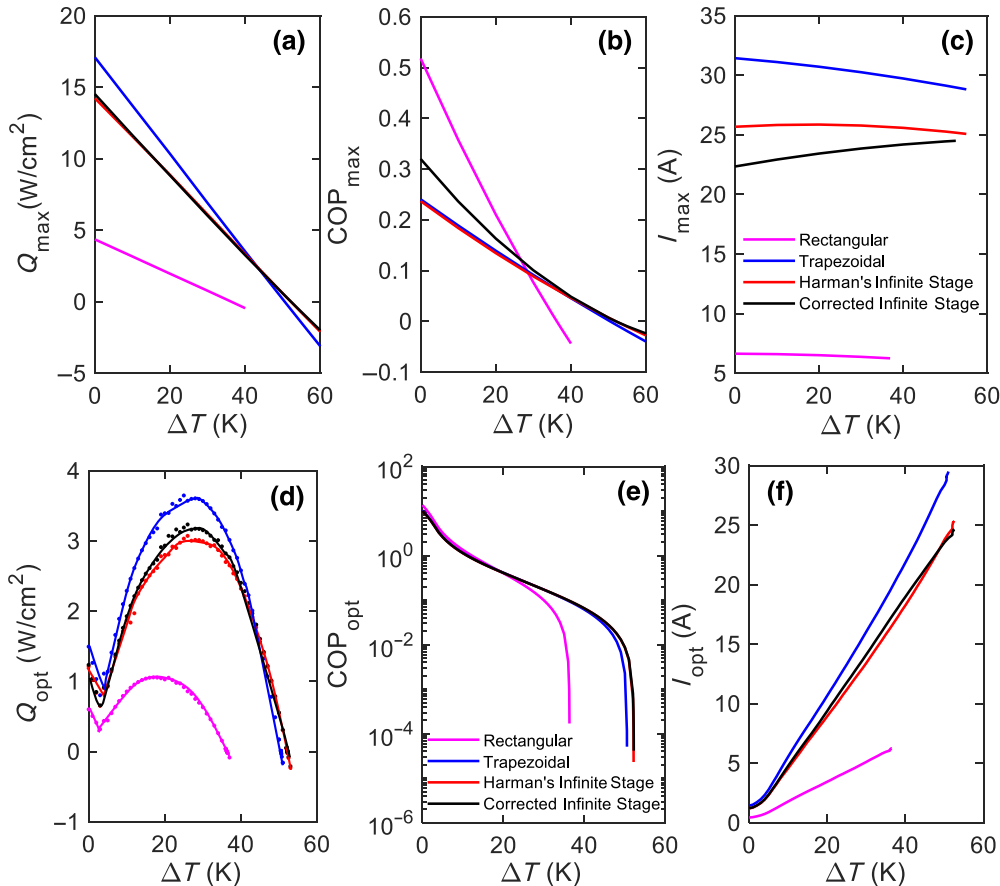


FIG. 8. (a) Maximum heat flow density versus temperature differential when the current is adjusted to achieve maximum  $Q$ , (b) COP at maximum heat flow density, (c) current density at maximum heat flow density, (d) optimum heat flow density versus temperature differential when the current is adjusted to achieve the maximum COP, (e)  $\text{COP}_{\text{opt}}$  versus temperature differential, and (f) the corresponding current.

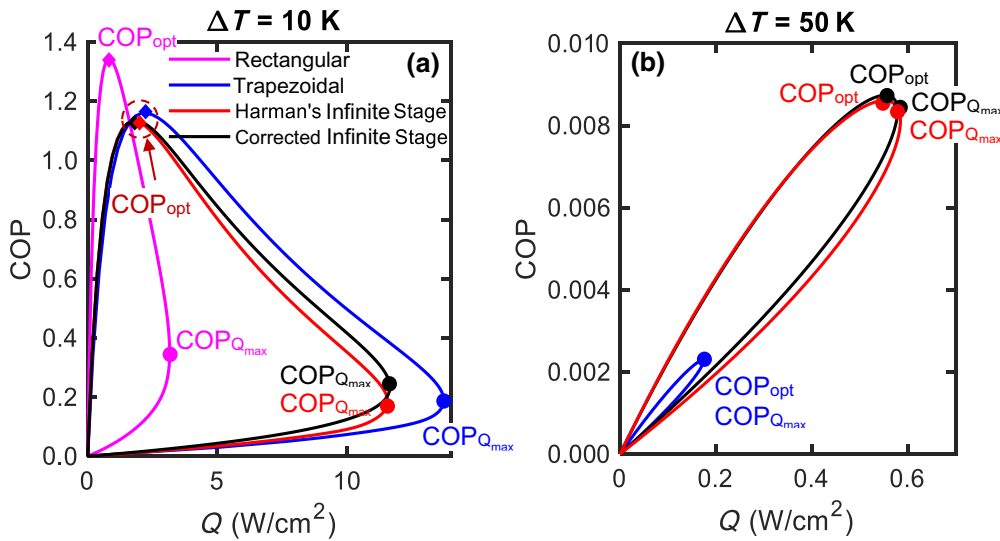


FIG. 9. COP versus heat flow density for different-shaped Nernst-Ettingshausen devices at (a)  $\Delta T = 10$  K and (b)  $\Delta T = 50$  K.

agrees with previous results [20]. We have not found any report of the COP values of other devices in the literature.

Optimum heat flow and COP show different trends in comparison with  $Q_{\max}$  and the  $COP_{Q_{\max}}$ . Optimum heat flow first increases with an increase in  $\Delta T$ , but for  $\Delta T > 30$  K, it shows a rapid decrease with a further rise in  $\Delta T$ . On the other hand, the  $COP_{\text{opt}}$  of all Ettingshausen devices at  $\Delta T < 20$  K show approximately similar values. At a lower temperature difference, the  $COP_{\text{opt}}$  is higher than unity for all devices, and it increases rapidly as  $\Delta T$  approaches zero, as also shown in Fig. 10. Above  $\Delta T = 25$  K, while the other devices exhibit approximately the same  $COP_{\text{opt}}$  values, they are significantly higher than the  $COP_{\text{opt}}$  of the rectangular device. This trend is expected as the other devices always carry higher heat flow density than the rectangular device. The trapezoidal device shows somewhat better performance in terms of  $Q_{\text{opt}}$  up to

$\Delta T \sim 40$  K at the cost of a higher current. At  $\Delta T > 40$ , however, the  $COP_{\text{opt}}$  of the trapezoidal device drops rapidly below those of the infinite-stage devices. The corrected infinite-stage device carries higher optimum heat flow at a slightly higher current than Harman's infinite-stage device while having an almost similar  $COP_{\text{opt}}$ .

Figures 10 and 11 illustrate the overall comparison of the device performance among differently shaped devices. Figure 10 demonstrates the COP and heat flow density with respect to the electric field and temperature difference. The COP as a function of the electric field and  $\Delta T$  is similar for all NE devices with a divergent point at lower electric fields and lower  $\Delta T$  values. The COP drops sharply with an increase in both the temperature difference and the electric field. On the other hand, the heat flow density as a function of the temperature difference and the electric field demonstrates similar trends observed in earlier

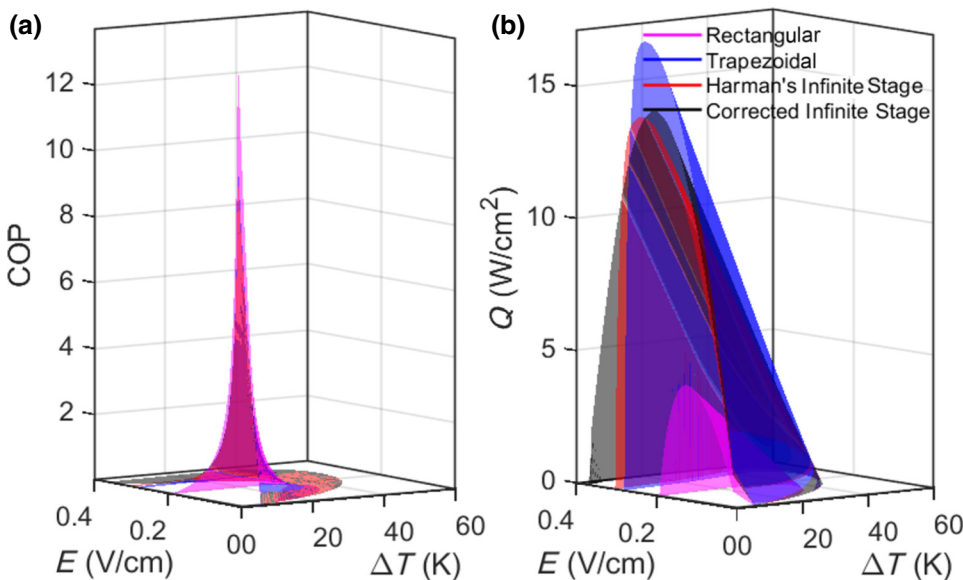


FIG. 10. (a) COP and (b) heat flow density as a function of applied electric field and temperature differential for differently shaped devices.

figures. The rectangular NE device provides less heat flow density, while the trapezoidal NE device shows greater heat-pump capability than the other devices at lower temperatures at the cost of a higher current. The corrected infinite-stage device is better in terms of the heat pump at a higher operating temperature differential. Figure 11 compares the temperature differential as a function of the COP and heat flow density for maximum COP and maximum  $Q$  for all the devices. The rectangular device shows similar characteristics of  $\Delta T$  for both conditions, while the other devices have different trends of  $\Delta T$  for the different conditions. Similar  $\Delta T_{\max}$  is obtained at maximum  $Q$  and maximum COP for each device. As in the earlier discussion, the infinite-stage devices show better performances at larger  $\Delta T$ , and the corrected infinite-stage device can carry more heat flow at a higher COP than the other devices. This improvement supports the argument that Harman's infinite-stage shaping expression was formulated on the basis of some simplifying assumptions, which overestimated the Joule heating of the device. Among all the geometries, the trapezoidal device gives consistent optimum performance in terms of the heat flow and the COP over the whole range of  $\Delta T$  at the cost of slightly smaller  $\Delta T_{\max}$ . The trapezoidal device, considering the complexity of making infinite-stage devices, could be a better option for practical cooling applications.

Figure 9 presents the COP versus heat flow density for different NE devices at  $\Delta T=10$  K and  $\Delta T=50$  K. According to Fig. 9, the trapezoidal NE device can give a higher heat flow density at  $\Delta T=10$  K than the other devices at the cost of higher current density at a particular COP. A similar characteristic is also observed in Fig. 8(a)

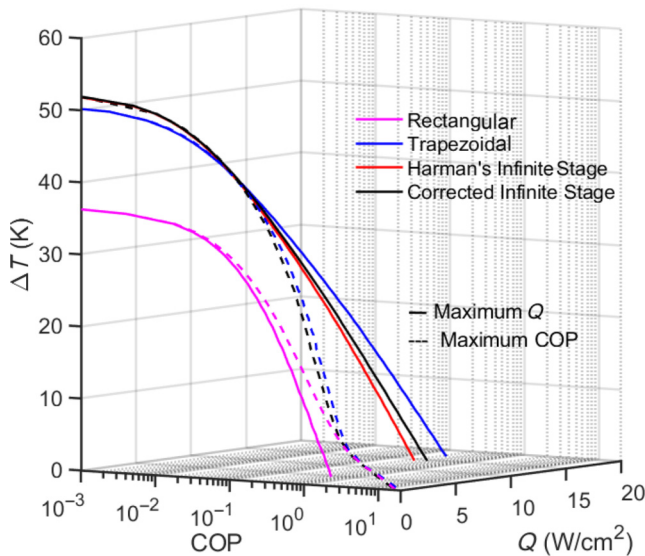


FIG. 11. Temperature differential as a function of the COP and heat flow density for different NE devices for maximum COP and maximum heat flow.

in that that the trapezoidal device can give higher heat flow at a specific temperature differential. As in Fig. 7, the  $COP_{Q_{\max}}$  and  $COP_{\text{opt}}$ , as shown in Fig. 9(a), are significantly different at small  $\Delta T$  values. This is usually not the case for TE or Peltier coolers. On the other hand, at larger  $\Delta T$ , the infinite-stage devices have a significantly higher COP with a higher heat flow density than the trapezoidal device. The corrected infinite-stage device has a slightly higher COP than Harman's infinite-stage device for the same heat flow density. Therefore, the corrected infinite-stage device shows overall better performance than the other devices of similar material at higher  $\Delta T$ . At higher  $\Delta T$ , the  $COP_{Q_{\max}}$  and  $COP_{\text{opt}}$  have similar values, which can also be seen in Fig. 11.

## V. CONCLUSION

The prospect of superconductors and spin-based applications in the cryogenic temperature range guided the scientific community to observe several exotic thermomagnetic effects coming from spin and quantum effects [42–44], which provide superior performance in solid-state cryocoolers [45,46]. We derive a modified expression for the shaping function of infinite stage Nernst-Ettingshausen coolers, which considers the temperature-dependent material resistivity, the device size, and the temperature conditions for designing a fully optimized cooler. In this derivation, some ideal assumptions made by Harman are corrected to obtain the modified infinite-stage-shape function. The corrected shape agrees with Harman's shape at zero temperature difference and for temperature-independent resistivity conditions and differs otherwise. A numerical model is further introduced that can consider all temperature-dependent material properties and for a device of any given shape. A case study based on Bi-Sb material is discussed to analyze and compare the performance of differently shaped coolers. The corrected infinite-stage device is found to be better in terms of the maximum heat flow density and COP at higher temperature differentials. A complete comparison of the device performance among differently shaped devices is provided to guide the selection of an optimum device structure based on the cost and applications. The trapezoidal device, while having a more-straightforward shape for fabrication purposes, can provide consistent cooling performance at the cost of a slightly lower temperature differential.

## ACKNOWLEDGMENTS

This work was partially supported by the U.S. National Science Foundation under Grants No. ECCS-1351533, No. ECCS-1515005, and No. ECCS-1711253, the U.S. Air Force Office of Scientific Research under Contract No. FA9550-19-1-0363, and the Oklahoma Center for Advancement in Science & Technology Applied Research, Project No. AR18-070, through Amethyst Research, Inc.

## APPENDIX: HARMAN'S DERIVATIONS FOR THE INFINITE-STAGE NE COOLER

On the basis of the energy-conservation principle, the rate of the output energy flow ( $\dot{\epsilon}$ ) from the  $(i+1)$ th stage should be equal to the sum of the rate of the input energy flow coming from the  $i$ th stage and the total power input ( $P$ ) to the  $(i+1)$ th stage. The conservation law also ensures that the output energy of the  $i$ th stage is equal to the input energy of the  $(i+1)$ th stage. Considering these relations, we can write the energy balance for the  $(i+1)$ th stage as

$$\dot{\epsilon}_{\text{out}}^{i+1} = P^{i+1} + \dot{\epsilon}_{\text{in}}^{i+1} = P^{i+1} + \dot{\epsilon}_{\text{out}}^i. \quad (\text{A1})$$

Considering,  $\dot{\epsilon}_{\text{out}}^i = \dot{\epsilon}^i$  and  $\dot{\epsilon}_{\text{in}}^{i+1} = \dot{\epsilon}^{i+1}$ , we can write Eq. (A1) as

$$\dot{\epsilon}^{i+1} = P^{i+1} + \dot{\epsilon}^i. \quad (\text{A2})$$

According to the definition of the COP of the  $(i+1)$ th stage (the COP is the ratio of the energy flow rate at the cold side and the input power), we can write

$$C^{i+1} = \frac{\dot{\epsilon}^i}{P^{i+1}} = \frac{\dot{\epsilon}^i}{\dot{\epsilon}^{i+1} - \dot{\epsilon}^i}. \quad (\text{A3})$$

Similarly, the COP for the  $i$ th stage can be written as

$$C^i = \frac{\dot{\epsilon}^{i-1}}{P^i} = \frac{\dot{\epsilon}^{i-1}}{\dot{\epsilon}^i - \dot{\epsilon}^{i-1}}. \quad (\text{A4})$$

Here,  $\Delta P^{i+1} = P^{i+1} - P^i$ . Therefore, Eq. (A3) can be rewritten as

$$C^{i+1} = \frac{\dot{\epsilon}^{i-1} + P^i}{P^i + \Delta P^{i+1}}. \quad (\text{A5})$$

To derive the optimum device shape, another essential assumption is the requirement of an equal individual COP among all the stages. Hence,  $C^{i+1} = C^i$ , which requires

$$C^i = \frac{P^i}{\Delta P^{i+1}} = \frac{P^i}{P^{i+1} - P^i}. \quad (\text{A6})$$

From Eqs. (A4) and (A6), a differential relation can be obtained as

$$\frac{dP}{P} = \frac{d\dot{\epsilon}}{\dot{\epsilon}}. \quad (\text{A7})$$

Moreover, for a parallelepiped-shaped NE stage (see Fig. 1), the input heat flux density ( $Q_{\text{in}}$ ) and input power ( $P$ )

can be found from the thermodynamic relations [40], and can be written as [20]

$$Q_{\text{in}} = \frac{E_y}{\rho_{yy}} B_z N_{yx} T_C - \frac{1}{2} \frac{E_y^2 a}{\rho_{yy}} - (1 - z_{yx} \bar{T}) \kappa_{xx} \frac{\Delta T}{a}, \quad (\text{A8})$$

$$P = \frac{E_y^2 a c}{\rho_{yy}} + \frac{B_z N_{yx}}{\rho_{yy}} \Delta T_C, \quad (\text{A9})$$

where  $E$  is the electric field,  $B$  is the magnetic field,  $\rho$  is the resistivity,  $\kappa$  is the thermal conductivity,  $N$  is the Nernst coefficient,  $T_C$  is the temperature on the cold side,  $T_L$  is the temperature on the hot side,  $\Delta T = T_L - T_C$  and  $\bar{T} = (T_L + T_C)/2$ ,  $z$  is the figure of merit, and  $a$ ,  $b$ , and  $c$  are the device length along the  $x$ ,  $y$ , and  $z$  axes, respectively. According to the definition, the COP can be written as

$$C = \frac{Q_{\text{in}} b c}{P}. \quad (\text{A10})$$

The COP in Eq. (A10) can be maximized for the optimum electric field, which provides a simplified expression for the optimum COP:

$$C_{\text{max}} = \frac{T_0}{\Delta T} \frac{(1 - \delta \frac{T_L}{T_0})}{(1 + \delta)} = \frac{T_0}{\Delta T} F(\delta). \quad (\text{A11})$$

To derive the optimum geometry, we must optimize the individual COP values [19]. From Eqs. (A4), (A6), and (A11), the final differential relation can be written as

$$\frac{dP}{P} = \frac{d\dot{\epsilon}}{\dot{\epsilon}} = \frac{dT}{TF(\delta)}. \quad (\text{A12})$$

Following steps similar to those given in Sec. II, a slightly different differential relation was obtained by Harman, which is [19]

$$\frac{dP}{P} = \frac{dz}{z} = \frac{d\dot{\epsilon}}{\dot{\epsilon}} = \frac{dT}{TF(\delta)} = b. \quad (\text{A13})$$

Again, based on conditions similar to those given in Sec. II, Harman's infinite-stage shaping function can be found from Eq. (A13), and is [19]

$$\ln \frac{z(x)}{z(0)} = \frac{x}{L_x} \ln \frac{z(L_x)}{z(0)}. \quad (\text{A14})$$

- 
- [1] M. S. Dresselhaus, G. Chen, M. Y. Tang, R. Yang, H. Lee, D. Wang, Z. Ren, J. P. Fleurial, and P. Gogna, New directions for low-dimensional thermoelectric materials, *Adv. Mater.* **19**, 1043 (2007).

- [2] A. Shakouri, Recent developments in semiconductor thermoelectric physics and materials, *Annu. Rev. Mater. Res.* **41**, 399 (2011).
- [3] I. Takeuchi and K. Sandeman, Solid-state cooling with caloric materials, *Phys. Today* **68**, 48 (2015).
- [4] A. Ziabari, M. Zebarjadi, D. Vashae, and A. Shakouri, Nanoscale solid-state cooling: A review, *Rep. Prog. Phys.* **79**, 095901 (2016).
- [5] F. J. DiSalvo, Thermoelectric cooling and power generation, *Science* **285**, 703 (1999).
- [6] M. M. H. Polash, Master's Thesis, North Carolina State University, Raleigh, NC, 2018.
- [7] Y. Zheng, T. Lu, Md M. H. Polash, M. Rasoulianboroujeni, N. Liu, M. E. Manley, Y. Deng, P. J. Sun, X. L. Chen, R. P. Hermann, D. Vashae, J. P. Heremans, and H. Zhao, Paramagnon drag yields a high thermoelectric figure of merit in Li-doped MnTe, *Sci. Adv.* **5**, eaat9461 (2019).
- [8] M. M. H. Polash, F. Mohaddes, M. Rasoulianboroujeni, and D. Vashae, Magnon-drag thermopower in antiferromagnets versus ferromagnets, *J. Mater. Chem. C* **8**, 4049 (2020).
- [9] M. M. H. Polash and D. Vashae, Magnon-bipolar carrier drag thermopower in antiferromagnetic/ferromagnetic semiconductors: Theoretical formulation and experimental evidence, *Phys. Rev. B* **102**, 045202 (2020).
- [10] M. M. H. Polash, M. Rasoulianboroujeni, and D. Vashae, Magnon and spin transition contribution in heat capacity of ferromagnetic Cr-doped MnTe: Experimental evidence for a paramagnetic spin-caloritronic effect, *Appl. Phys. Lett.* **117**, 043903 (2020).
- [11] H. J. Goldsmid, *The Physics of Thermoelectric Energy Conversion* (Morgan & Claypool Publishers, San Rafael, CA, 2017), pp. 2-7-2-8.
- [12] A. Miura, H. S. Amin, K. Masuda, H. Tsuchiura, Y. Miura, R. Iguchi, Y. Sakuraba, J. Shiomi, K. Hono, and K.-I. Uchida, Observation of anomalous ettingshausen effect and large transverse thermoelectric conductivity in permanent magnets, *Appl. Phys. Lett.* **115**, 222403 (2019).
- [13] K. Behnia, M.-A. Méasson, and Y. Kopelevich, Oscillating Nernst-Ettingshausen Effect in Bismuth Across the Quantum Limit, *Phys. Rev. Lett.* **98**, 166602 (2007).
- [14] R. Modak and K.-I. Uchida, Enhancement of temperature change induced by anomalous ettingshausen effect in thin Ni films on suspended membrane substrates, *Appl. Phys. Lett.* **116**, 032403 (2020).
- [15] A. Miura, R. Iguchi, T. Seki, K. Takanashi, and K.-I. Uchida, Spin-mediated charge-to-heat current conversion phenomena in ferromagnetic binary alloys, *Phys. Rev. Mater.* **4**, 034409 (2020).
- [16] O. Yamashita and S. Tomiyoshi, Effect of geometrical shape on magneto-peltier and ettingshausen cooling in Bi and Bi<sub>0.88</sub>Sb<sub>0.12</sub> polycrystals, *J. Appl. Phys.* **92**, 3794 (2002).
- [17] R. Ando and T. Komine, Geometrical contribution to the anomalous Nernst effect in TbFeCo thin films, *AIP Adv.* **8**, 056326 (2018).
- [18] O. Yamashita, K. Satou, and S. Tomiyoshi, Geometrical effect in magneto-Peltier cooling of single crystal Bi, *J. Appl. Phys.* **95**, 8233 (2004).
- [19] T. C. Harman, Theory of the infinite stage Nernst-Ettingshausen refrigerator, *Adv. Energy Convers.* **3**, 667 (1963).
- [20] S. R. Hawkins, C. F. Kooi, K. F. Cuff, J. L. Weaver, R. B. Horst, and G. M. Enslow, in *Advances in Cryogenic Engineering*, edited by K. D. Timmerhaus (Springer, Boston, 1964), Vol. 9, pp. 367-378.
- [21] S. Sugimoto, Current status and recent topics of rare-earth permanent magnets, *J. Phys. D* **44**, 064001 (2011).
- [22] R. H. Richman and W. P. McNaughton, Permanent-Magnet materials: Research directions and opportunities, *J. Electron. Mater.* **26**, 415 (1997).
- [23] A. Nozariasbmarz, H. Collins, K. Dsouza, M. M. H. Polash, M. Hosseini, M. Hyland, J. Liu, A. Malhotra, F. M. Ortiz, F. Mohaddes, V. P. Ramesh, Y. Sargolzaeiaval, N. Snouwaert, M. C. Öztürk, and D. Vashae, Review of wearable thermoelectric energy harvesting: From body temperature to electronic systems, *Appl. Energy* **258**, 114069 (2020).
- [24] A. Gharleghi, M. M. H. Polash, R. Malekfar, S. Aminoroaya Yamini, and D. Vashae, Influence of the order of fabrication sequences on the thermoelectric properties of skutterudite CoSb<sub>3</sub>-Cu<sub>0.6</sub>Ni<sub>0.4</sub> nanocomposites, *J. Alloys Compd.* **845**, 156188 (2020).
- [25] J. P. Heremans, in *Proc. SPIE, 9821, Tri-Technology Device Refrigeration (TTDR)* (2016), pp. 98210G.
- [26] R. Venkatasubramanian, Cascade cryogenic thermoelectric cooler for cryogenic and room temperature applications, US Patent, US6505468B2, (2003).
- [27] S. Karabetoglu, A. Sisman, Z. F. Ozturk, and T. Sahin, Characterization of a thermoelectric generator at low temperatures, *Energy Convers. Manage.* **62**, 47 (2012).
- [28] T. A. Cain, A. P. Kajdos, and S. Stemmer, La-doped SrTiO<sub>3</sub> films with large cryogenic thermoelectric power factors, *Appl. Phys. Lett.* **102**, 182101 (2013).
- [29] C.-J. Hsu, S. M. Sandoval, K. P. Wetzlar, and G. P. Carman, Thermomagnetic conversion efficiencies for ferromagnetic materials, *J. Appl. Phys.* **110**, 123923 (2011).
- [30] L.-D. Zhao, C. Chang, G. Tan, and M. G. Kanatzidis, SnSe: A remarkable new thermoelectric material, *Energy Environ. Sci.* **9**, 3044 (2016).
- [31] L.-D. Zhao, J. He, D. Berardan, Y. Lin, J.-F. Li, C.-W. Nan, and N. Dragoe, Bicusse oxyselenides: New promising thermoelectric materials, *Energy Environ. Sci.* **7**, 2900 (2014).
- [32] M. Zebarjadi, Thermomagnetic transport in polycrystalline samples, *J. Electron. Mater.* **44**, 3827 (2015).
- [33] Marcel Gueltig, Frank Wendler, Hinnerk Ossmer, Makoto Ohtsuka, Hiroyuki Miki, Toshiyuki Takagi, and Manfred Kohl, High-performance thermomagnetic generators based on heusler alloy films, *Adv. Energy Mater.* **7**, 1601879 (2017).
- [34] K. Behnia, M.-A. Measson, and Y. Kopelevich, Nernst Effect in Semimetals: The Effective Mass and the Figure of Merit, *Phys. Rev. Lett.* **98**, 076603 (2007).
- [35] L. Medici, Thermomagnetic Mechanism for Self-Cooling Cables, *Phys. Rev. Appl.* **5**, 024001 (2016).
- [36] C. F. Kooi, R. B. Horst, and K. F. Cuff, Thermoelectric-thermomagnetic energy converter staging, *J. Appl. Phys.* **39**, 4257 (1968).
- [37] C. F. Kooi, R. B. Horst, K. F. Cuff, and S. R. Hawkins, Theory of the longitudinally isothermal ettingshausen cooler, *J. Appl. Phys.* **34**, 1735 (1963).
- [38] K. Scholz, P. Jandl, U. Birkholz, and Z. M. Dashevskii, Infinite stage ettingshausen cooling in Bi-Sb alloys, *J. Appl. Phys.* **75**, 5406 (1994).

- [39] K. F. Cuff, R. B. Horst, J. L. Weaver, S. R. Hawkins, C. F. Kooi, and G. M. Enslow, The thermomagnetic figure of merit and ettingshausen cooling in Bi-Sb alloys, *Appl. Phys. Lett.* **2**, 145 (1963).
- [40] T. C. Harman, J. M. Honig, and B. M. Tarmy, Galvano-Thermomagnetic phenomena. IV. application to anisotropic adiabatic nernst generators, *J. Appl. Phys.* **34**, 2215 (1963).
- [41] R. T. Delves, Figure of merit for ettingshausen cooling, *Br. J. Appl. Phys.* **15**, 105 (1964).
- [42] S. Meyer, Y.-T. Chen, S. Wimmer, M. Althammer, T. Wimmer, R. Schlitz, S. Geprägs, H. Huebl, D. Ködderitzsch, H. Ebert, G. E. W. Bauer, R. Gross, and S. T. B. Goennenwein, Observation of the spin nernst effect, *Nat. Mater.* **16**, 977 (2017).
- [43] C.-Y. Hou, K. Shtengel, G. Refael, and P. M. Goldbart, Ettingshausen effect due to majorana modes, *New J. Phys.* **14**, 105005 (2012).
- [44] S. Ullah and A. T. Dorsey, Critical Fluctuations in High-Temperature Superconductors and the Ettingshausen Effect, *Phys. Rev. Lett.* **65**, 2066 (1990).
- [45] A. Sakai, S. Minami, T. Koretsune, T. Chen, T. Higo, Y. Wang, T. Nomoto, M. Hirayama, S. Miwa, D. Nishio-Hamane, F. Ishii, R. Arita, and S. Nakatsuji, Iron-based binary ferromagnets for transverse thermoelectric conversion, *Nature* **581**, 53 (2020).
- [46] K. Gopinadhan, Y. J. Shin, R. Jalil, T. Venkatesan, A. K. Geim, A. H. Castro Neto, and H. Yang, Extremely large magnetoresistance in few-layer graphene/boron–nitride heterostructures, *Nat. Commun.* **6**, 8337 (2015).